Supplementary Materials

Realizing High Power Factor and Thermoelectric Performance in Band Engineered AgSbTe₂

Yu Zhang,[1,2,§] Congcong Xing,[1,2,§] Dongyang Wang,[3] Aziz Genç,[4] Seng Huat Lee,[5,6] Cheng Chang,[7] Zhi Li,[8] Luyao Zheng,[2] Khak Ho Lim,[9] Hangtian Zhu,[2,10] Rabeya Bosry Smriti,[2,11] Yu Liu,[12] Shaobo Cheng,[3] Min Hong,[13] Xiaolei Fan,[1, 14] Zhiqiang Mao,[5,6] Li-Dong Zhao,[7] Andreu Cabot,[15,16] Tiejun Zhu,[1,17]* Bed Poudel,[2]**

*Corresponding author

Email: yzhangpeter@163.com (Y.Z.); zhutj@zju.edu.cn (T.Z); bup346@psu.edu (B.P.);

[1]Institute of Wenzhou, Zhejiang University, Wenzhou 325006, China

[2]Department of Materials Science and Engineering, Pennsylvania State University, University Park, Pennsylvania 16802, United States

[3]Henan Key Laboratory of Diamond Optoelectronic Materials and Devices, Key Laboratory of Material Physics, Ministry of Education, School of Physics, Zhengzhou University, Zhengzhou 450052, China

[4]Cardiff Catalysis Institute, School of Chemistry, Cardiff University, Cardiff CF10 3AT, UK

[5]2D Crystal Consortium, Materials Research Institute, The Pennsylvania State University, University Park, Pennsylvania 16802, United States

[6]Department of Physics, The Pennsylvania State University, University Park, Pennsylvania 16802, United States

[7]School of Materials Science and Engineering, Beihang University, Beijing 100191, China

[8]Department of Materials Science and Engineering, Northwestern University, Evanston, Illinois 60208, United States

[9]Institute of Zhejiang University-Quzhou, Quzhou 324000, China

[10]Beijing National Laboratory for Condensed Matter Physics, Institute of Physics, Chinese Academy of Sciences, Beijing 100190, China

[11]Department of Mechanical Engineering, Pennsylvania State University, University Park, Pennsylvania 16802, United States

[12]Anhui Province Key Laboratory of Advanced Catalytic Materials and Reaction Engineering, School of Chemistry and Chemical Engineering, Hefei University of Technology, Hefei 230009, China

[13]Centre for Future Materials, and School of Engineering, University of Southern Queensland, Springfield Central, Queensland 4300, Australia

[14]Department of Chemical Engineering, School of Engineering, The University of Manchester, Oxford Road, Manchester M13 9PL, United Kingdom

[15]Catalonia Institute for Energy Research-IREC, Sant Adrià de Besòs, Barcelona 08930, Catalonia, Spain

[16]ICREA, Pg. Lluis Companys, 08010 Barcelona, Catalonia, Spain

[17]State Key Laboratory of Silicon and Advanced Semiconductor Materials, and School of Materials Science and Engineering, Zhejiang University, Hangzhou 310058, China

§These authors contributed equally to this work.
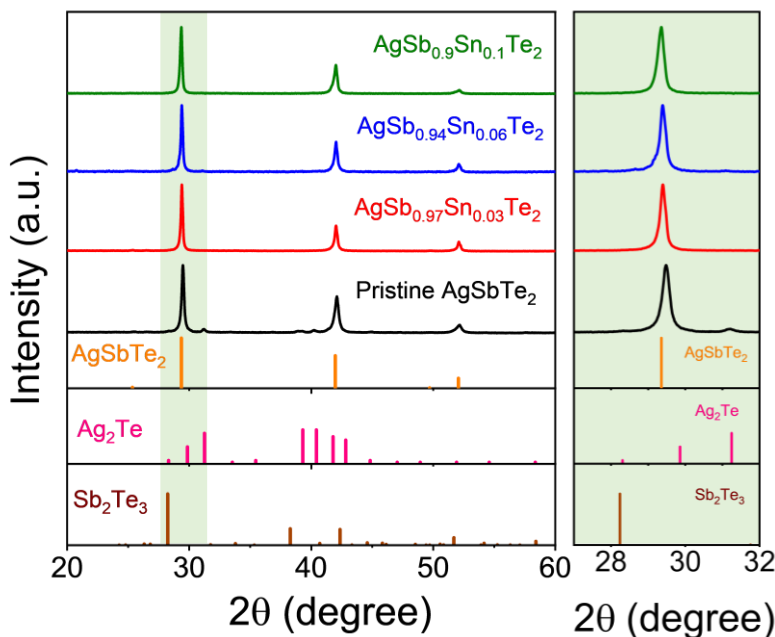
Supplementary Figure 1. XRD pattern of AgSb$_{1-x}$Sn$_x$Te$_2$ pellets. XRD patterns of as-synthesized AgSb$_{1-x}$Sn$_x$Te$_2$ pellets and the magnification of the XRD pattern showing a clear Ag$_2$Te peak in the pristine AgSbTe$_2$ sample.
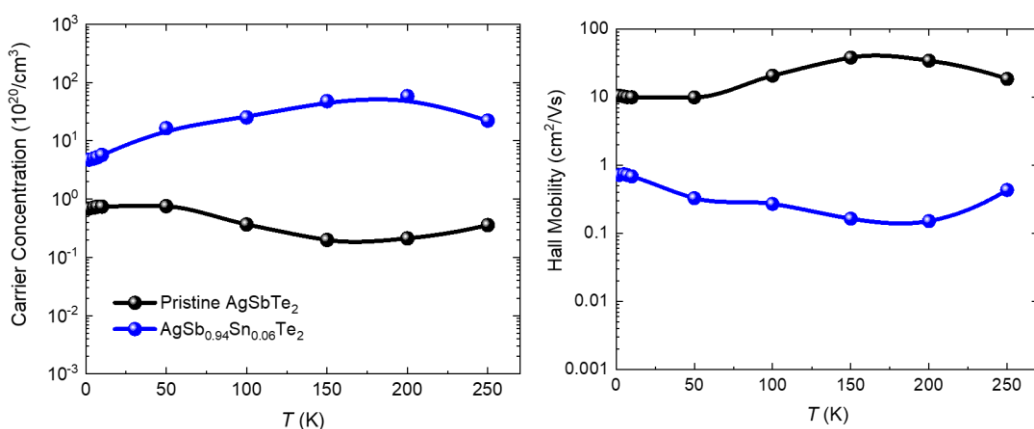
Supplementary Figure 2. Low temperature hall transport properties. Temperature-dependent carrier concentrations and mobility in pristine AgSbTe$_2$ and AgSb$_{0.94}$Sn$_{0.06}$Te$_2$.
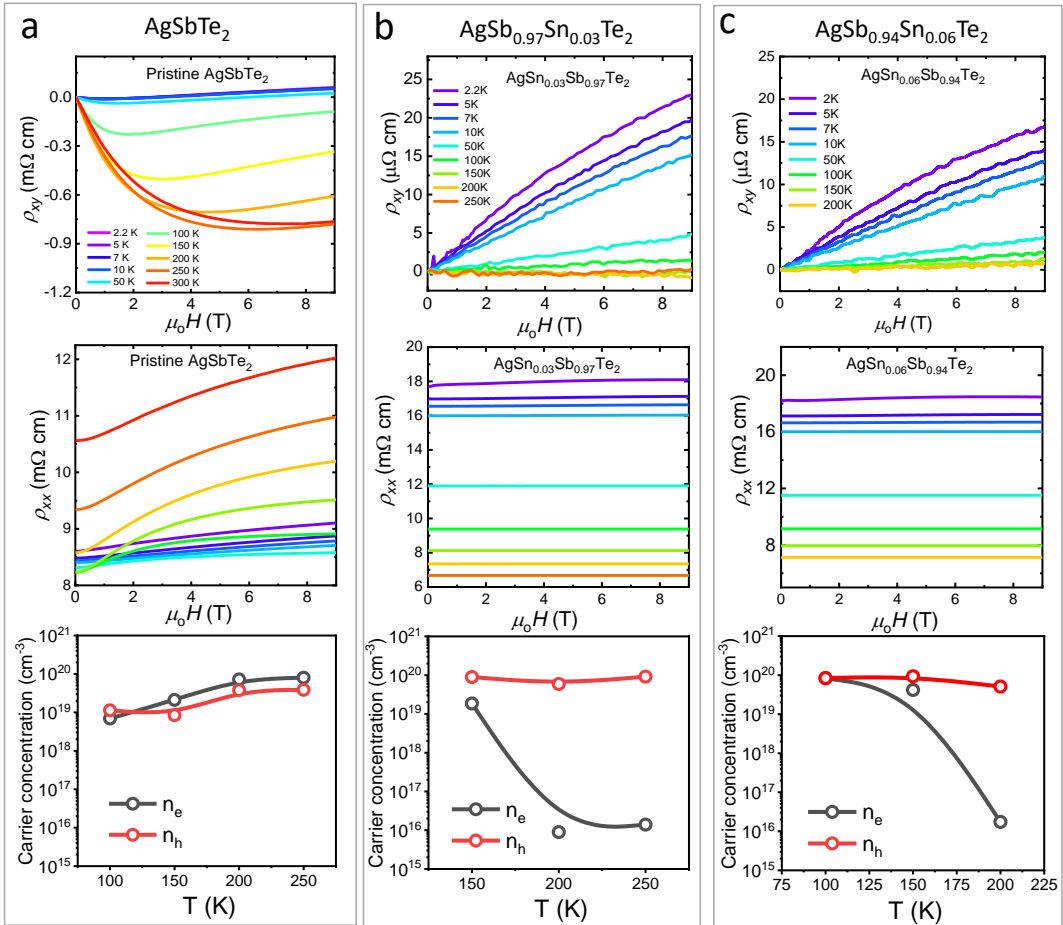
**Supplementary Figure 3**. **Carrier density simulated from two-carrier model.** Representative field-dependent Hall resistivity (ρ_{xy}), longitudinal resistivity (ρ_{xx}) and calculated concentration of electrons (n_e) and holes (n_h) by two band model at different temperatures. (A) pristine $AgSbTe_2$; (B) $AgSb_{0.97}Sn_{0.03}Te_2$ sample; (C) $AgSb_{0.94}Sn_{0.06}Te_2$ sample.

Given that $AgSbTe_2$ contains two types of carriers, the accurate concentrations (Figure S3) of electrons and holes requires two-carrier model to evaluate the impact of Sn doping on each carrier. The concentrations of both electrons and holes were estimated using two-carrier model and equation from previous works[1,2]:

$$\sigma_{xy} = \frac{\rho_{xy}}{\rho_{xx}^2 + \rho_{xy}^2} = \left[\frac{-n_e \mu_e^2}{1 + (\mu_e B)^2} + \frac{n_h \mu_h^2}{1 + (\mu_h B)^2} \right] e\mathbf{B}$$

Where ρ_{xx}, ρ_{xy} and **B** are longitudinal resistivity, Hall resistivity and magnetic field strength measured from PPMS. In pristine $AgSbTe_2$, the hole concentration (n_h) presents consistently lower values than the electron concentration (n_e) when T>100 K, aligning with previous reports of negative Hall coefficients in $AgSbTe_2$ at room temperature.[3] However, upon Sn doping, a

significant increase in hole concentration was observed, reaching 9×10^{19} cm^{-3} in AgSb$_{0.97}$Sn$_{0.03}$Te$_2$ sample, with all doped samples showing higher n_h than n_e.
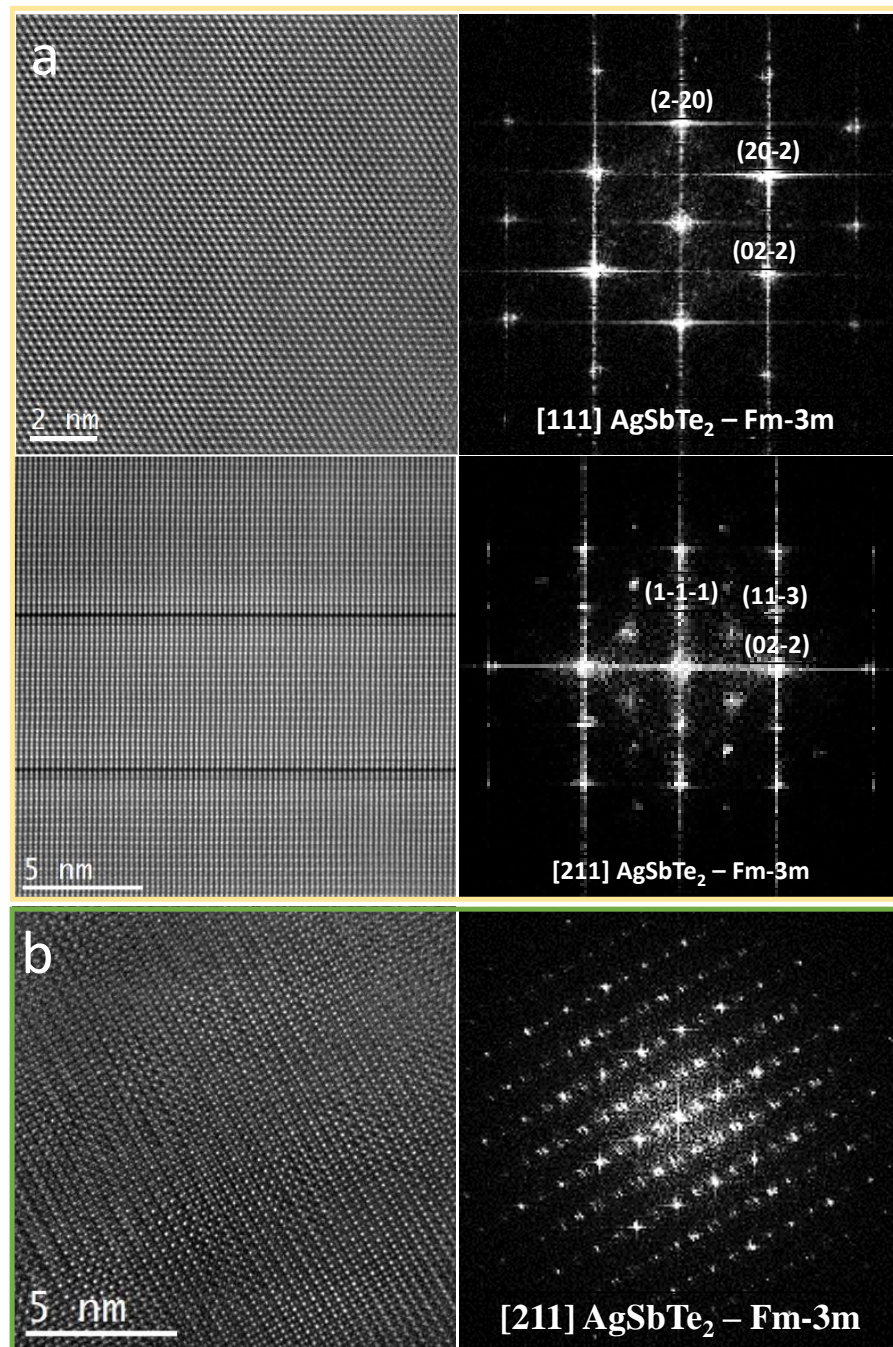

Supplementary Figure 4. **Microstructure characterization.** Atomic resolution HAADF-STEM micrograph and FFT pattern of (a) pritstine AgSbTe$_2$ and (b) AgSb$_{0.94}$Sn$_{0.06}$Te$_2$ samples visualized along its [111]/[211] zone axis.
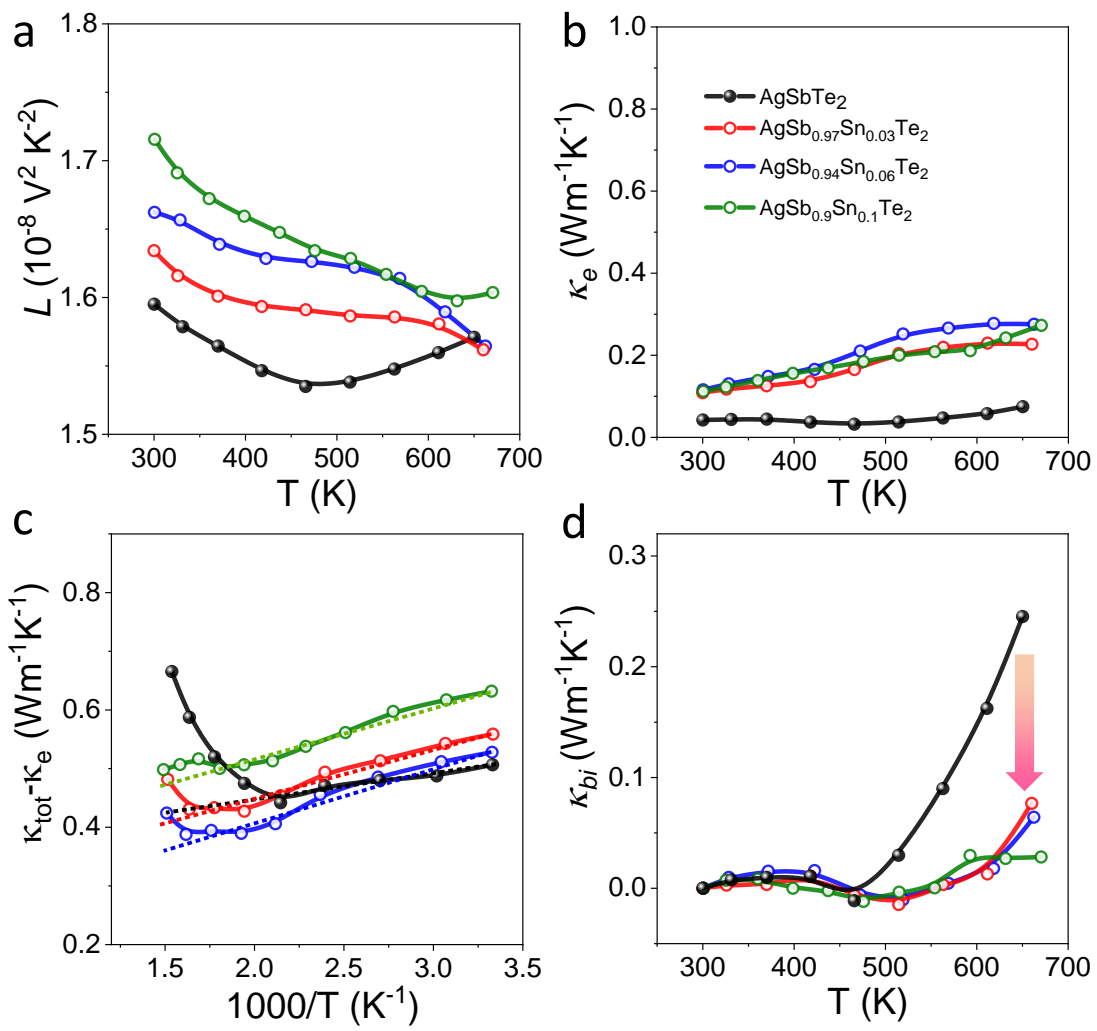
**Supplementary Figure 5. Lorenz number and thermal conductivity calculation.** Temperature dependence of (a) Lorenz number, L; (b) electronic thermal conductivity (κ_e); (c) Subtraction of the electronic thermal conductivity from total thermal conductivity (κ_{tot}-κ_e) and (d) bipolar thermal conductivity (κ_{bi}) of polycrystalline AgSb$_{1-x}$Sn$_x$Te$_2$ samples.
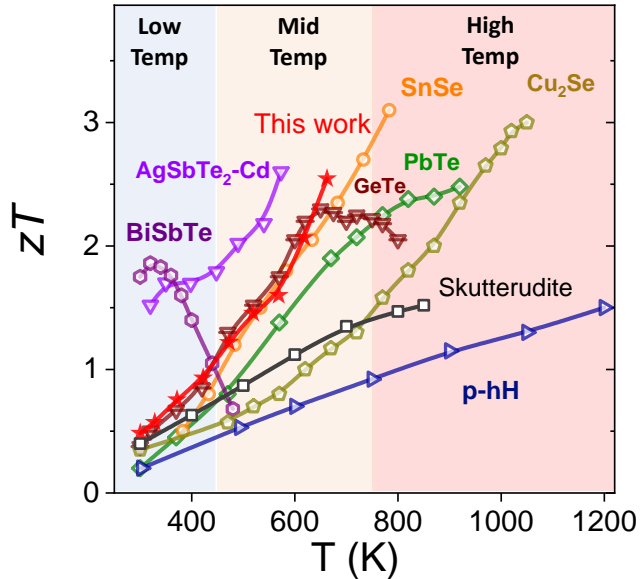
Supplementary Figure 6. **TE performance comparison.** zT comparison with state-of-art TE materials across low-, middle- and high-temperature regimes.[4-11]
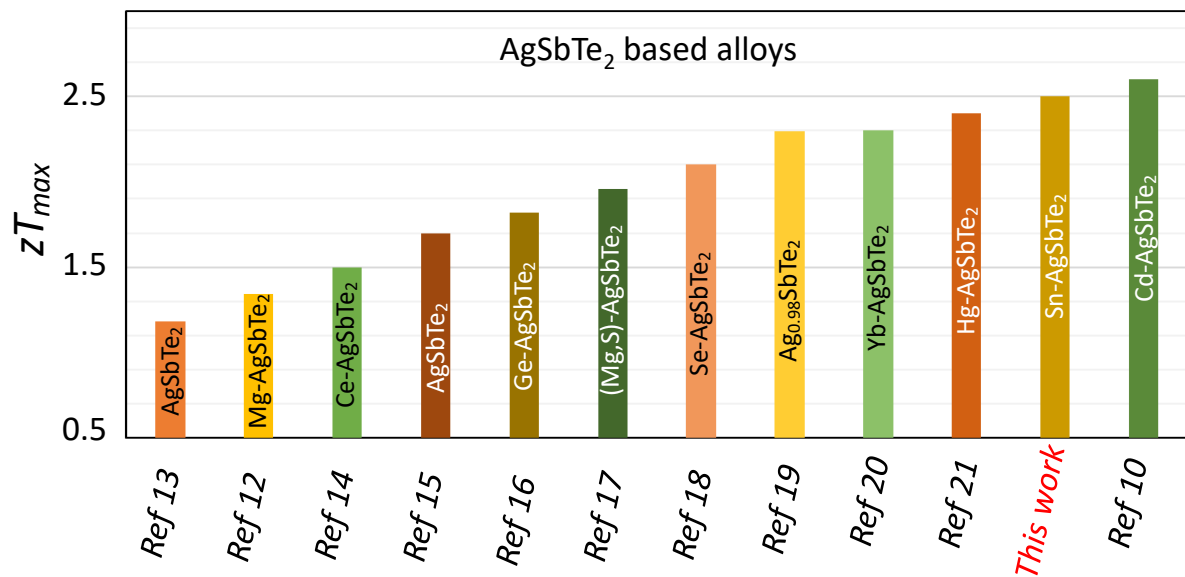

Supplementary Figure 7. Maximum zT comparison. Comparison of the maximum figure of merit, zT_{max}, of AgSb$_{0.94}$Sn$_{0.06}$Te$_2$ with other reported AgSbTe$_2$-based materials.[10,12-21]
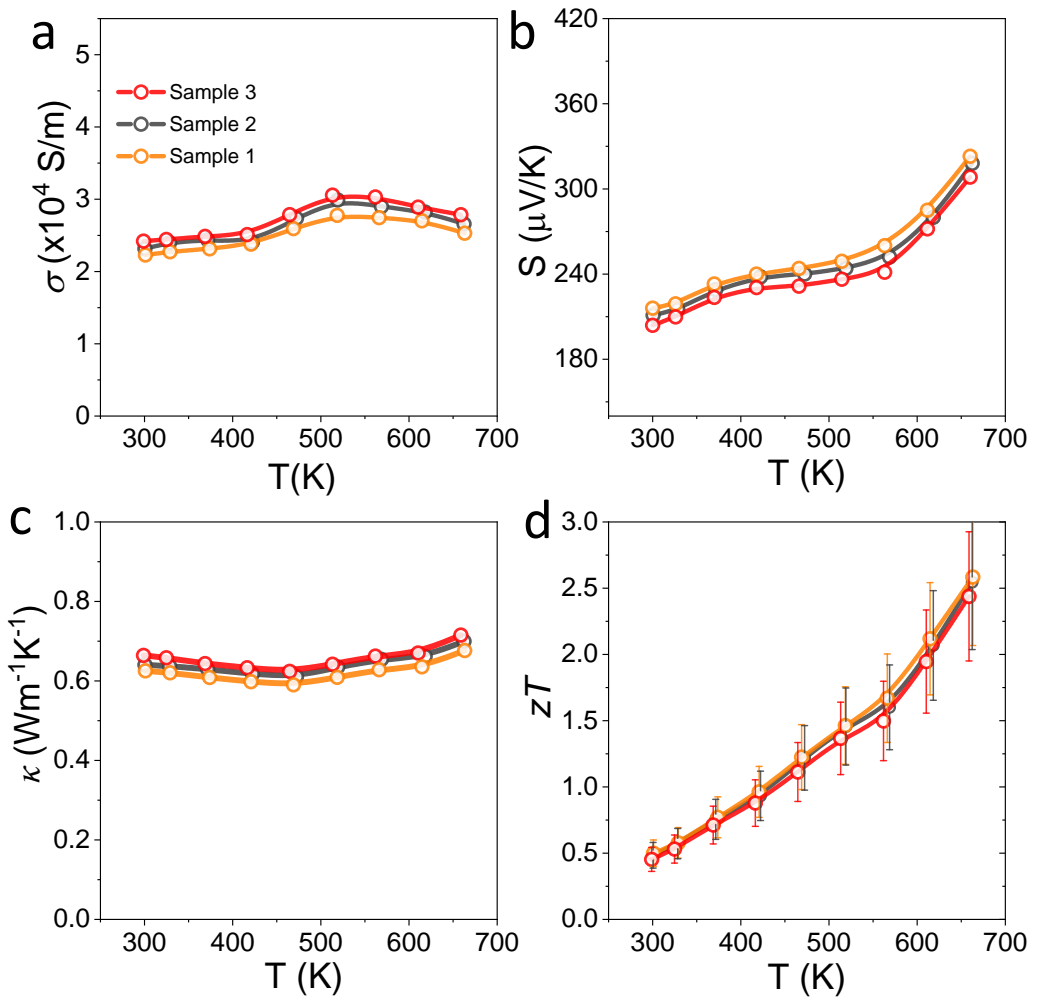
**Supplementary Figure 8. Reproducibility of TE properties on three AgSb$_{0.94}$Sn$_{0.06}$Te$_2$ samples.** Temperature dependent TE performance of (a) electrical conductivity (σ), (b) Seebeck coefficient (S), (c) total thermal conductivity (κ) and (d) TE figure of merit (zT), the uncertainty of zT measurement is ~20% as indicated by error bar.
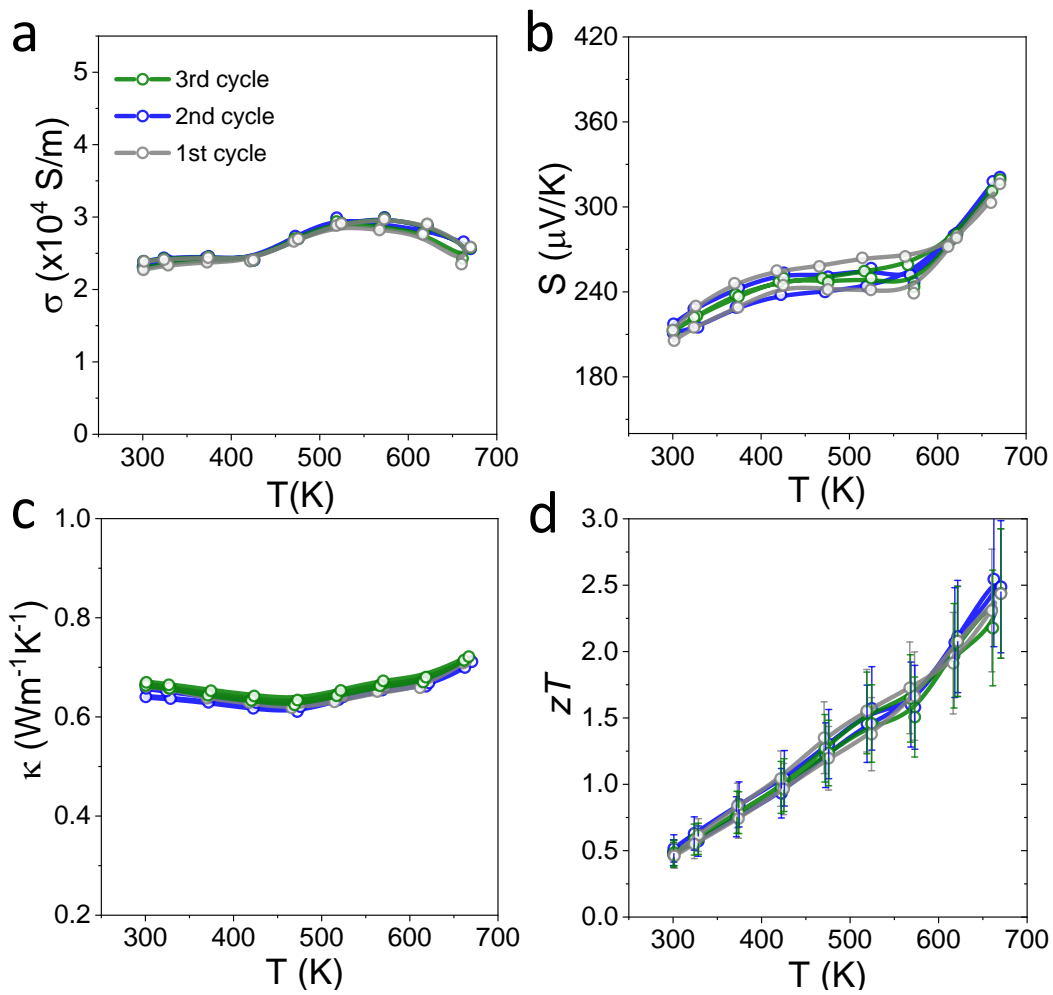
Supplementary Figure 9. Reversibility of TE properties of AgSb$_{0.94}$Sn$_{0.06}$Te$_2$ with three heating-cooling cycles. Temperature-dependent TE performance: (a) electrical conductivity (σ), (b) Seebeck coefficient (S), (c) total thermal conductivity (κ) and (d) TE figure of merit (zT), the uncertainty of zT measurement is ~20% as indicated by error bar.
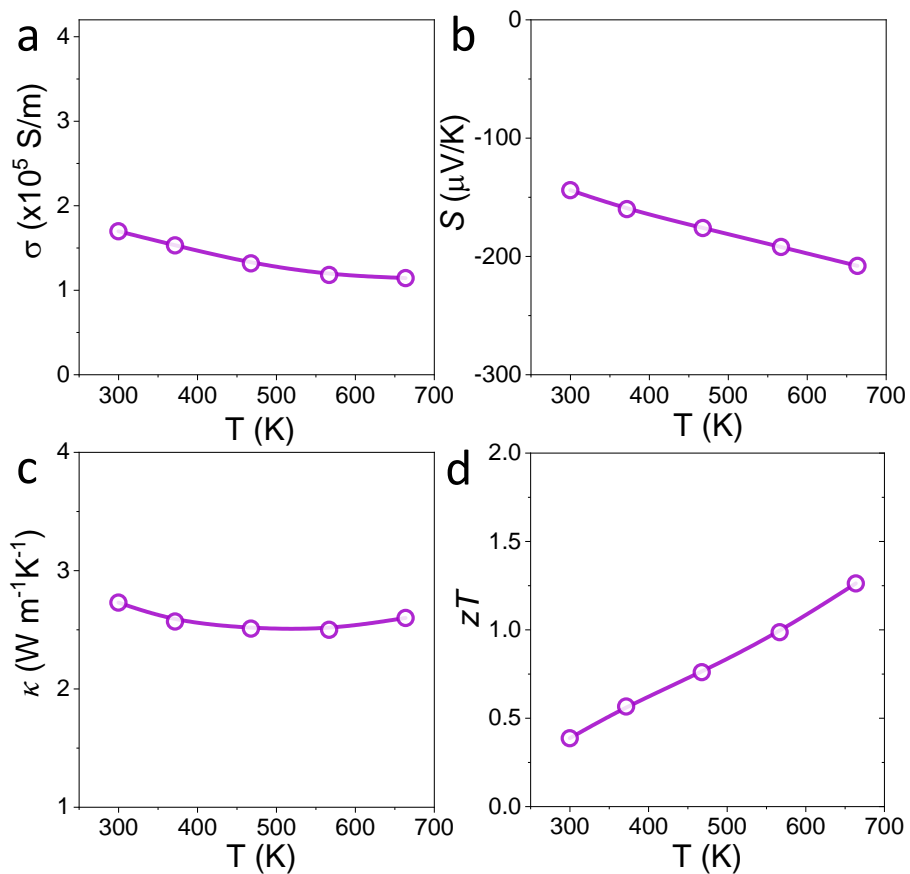
Supplementary Figure 10. Thermoelectric properties of n-leg Yb$_{0.25}$Co$_{3.75}$Fe$_{0.25}$Sb$_{12}$. TE properties of Yb$_{0.25}$Co$_{3.75}$Fe$_{0.25}$Sb$_{12}$ skutterudite woking as a n-leg. Temperature-dependent TE performance: (a) electrical conductivity (σ), (b) Seebeck coefficient (S), (c) total thermal conductivity (κ) and (d) TE figure of merit (zT).
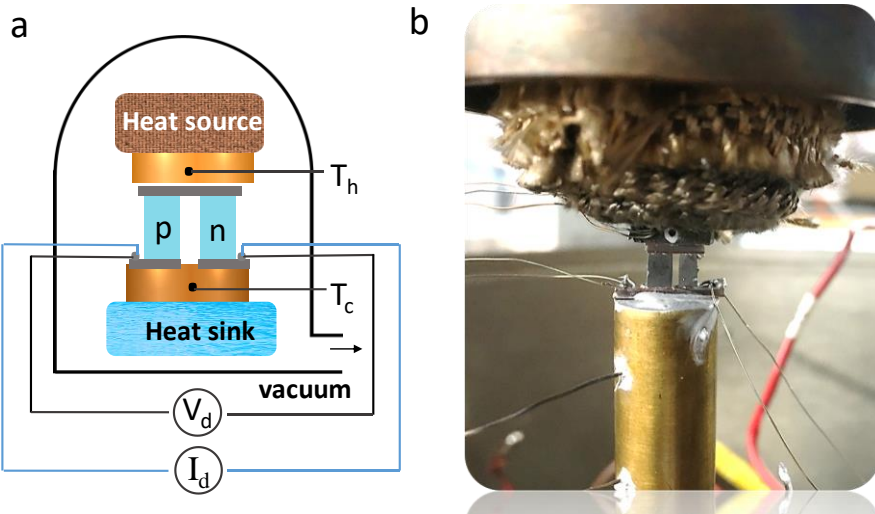
**Supplementary Figure 11. Power generation test.** (a) Schematic diagram of the unicouple measurement and (b) photograph of the fabricated device and the power generation measurement setup.
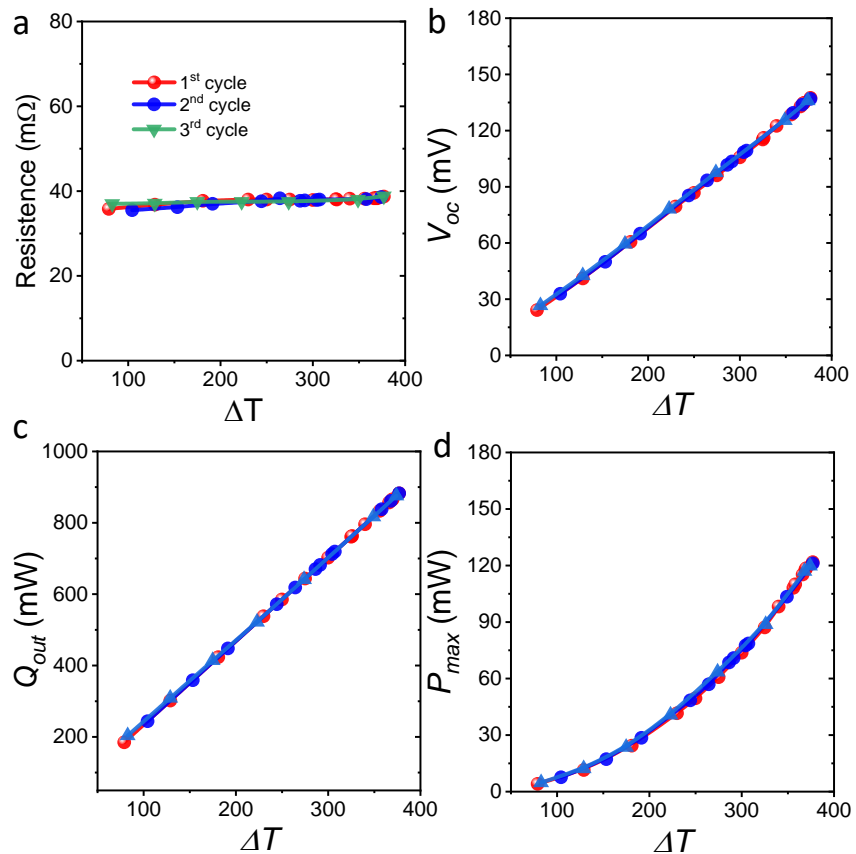
Supplementary Figure 12. Cyclic performance of the unicouple device. (a) Resistance; (b) Open circuit voltage (V_{oc}); (c) heat flow (Q_{out}); (d) maximum output power (P_{max}) as a function of ΔT.
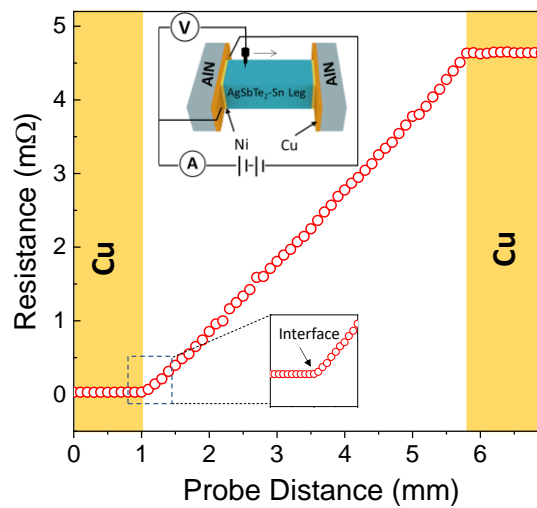
Supplementary Figure 13. Contact resistance measurement. The schematic diagram of home-made four-probe contact resistance measurement system and the contact resistance plots of $AgSb_{0.94}Sn_{0.06}Te_2$ leg.
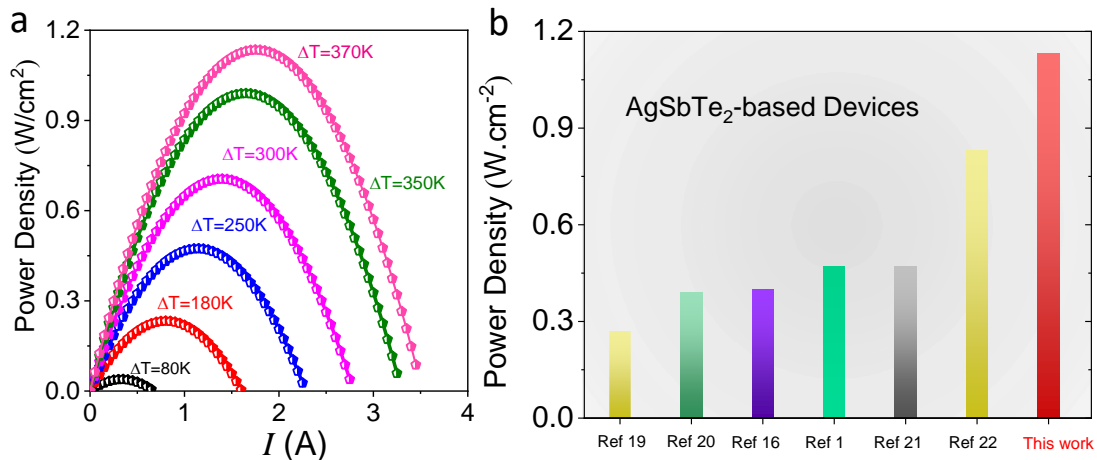
Supplementary Figure 14. Power density of unicouple devices. (a) Current-dependent power density of fabricated $AgSb_{0.94}Sn_{0.06}Te_2$ unicouple module. (b) Power density comparison of state-of-art $AgSbTe_2$ based devices[1,16,19-22].
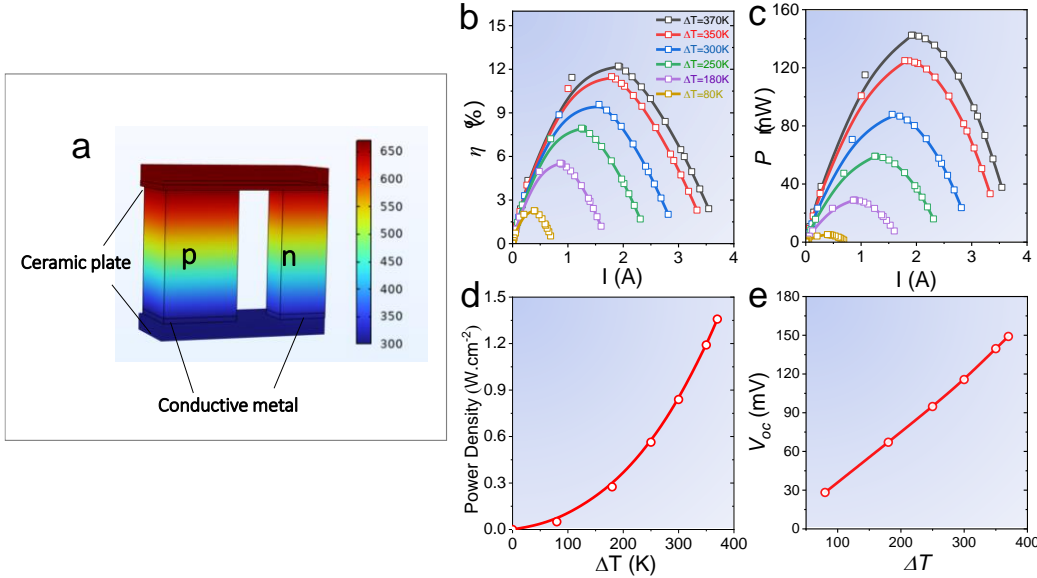
**Supplementary Figure 15**. **COMSOL Multiphysics Simulation.** (a) Schematic illustration of the simulated unicouple device made of $AgSb_{0.94}Sn_{0.06}Te_2$ leg and $Yb_{0.25}Co_{3.75}Fe_{0.25}Sb_{12}$ leg. (b) Simulated current-dependent conversion efficiency (η_{max}) and (c) output power (P_{max}) of the unicouple. (d) Simulated maximum power density and (e) open circuit voltage as a function of ΔT.
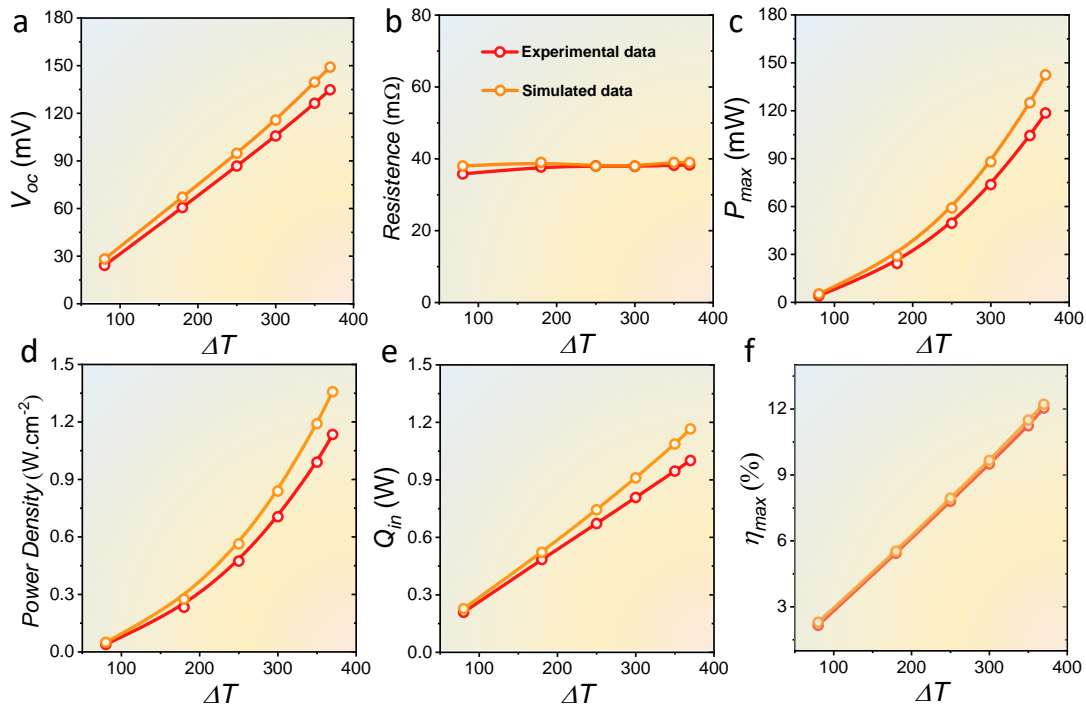
Supplementary Figure 15-2. **Data comparison.** Comparison of experimental data (red color) with the data from COMSOL Multiphysics simulation software (orange color) on the unicouple device made of $AgSb_{0.94}Sn_{0.06}Te_2$ leg and $Yb_{0.25}Co_{3.75}Fe_{0.25}Sb_{12}$ leg: (a) open-circuit voltage, V_{oc}; (b) internal resistance; (c) power output, P_{max}; (d) power density; (e) heat flow, Q_{in} and (f) efficiency, η_{max}.
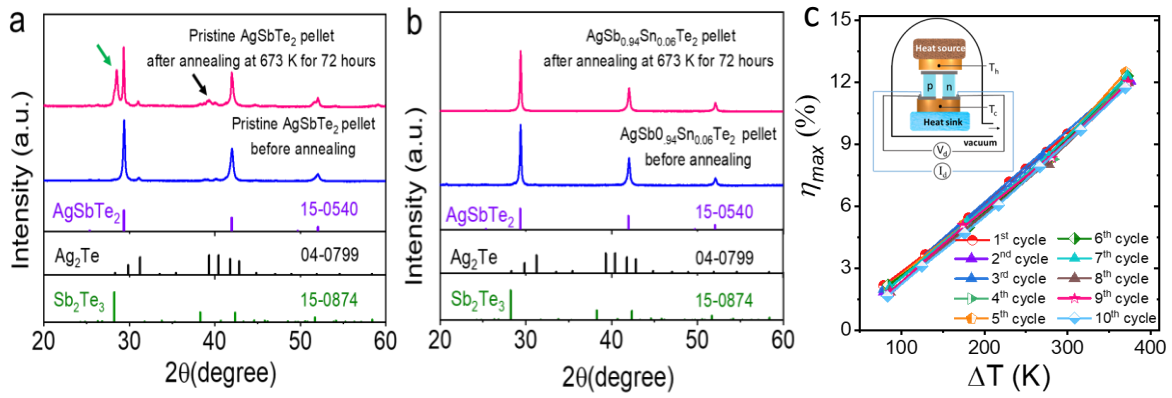
Supplementary Figure 16. **Stability Assessment.** XRD patterns of (a) pristine $AgSbTe_2$ and (b) $AgSb_{0.94}Sn_{0.06}Te_2$ samples before and after annealing in argon atmosphere at 673 K for 72 hours. (c) Cyclic test on the unicouple device after thermal cycling between 373 K and 673 K for ten cycles.
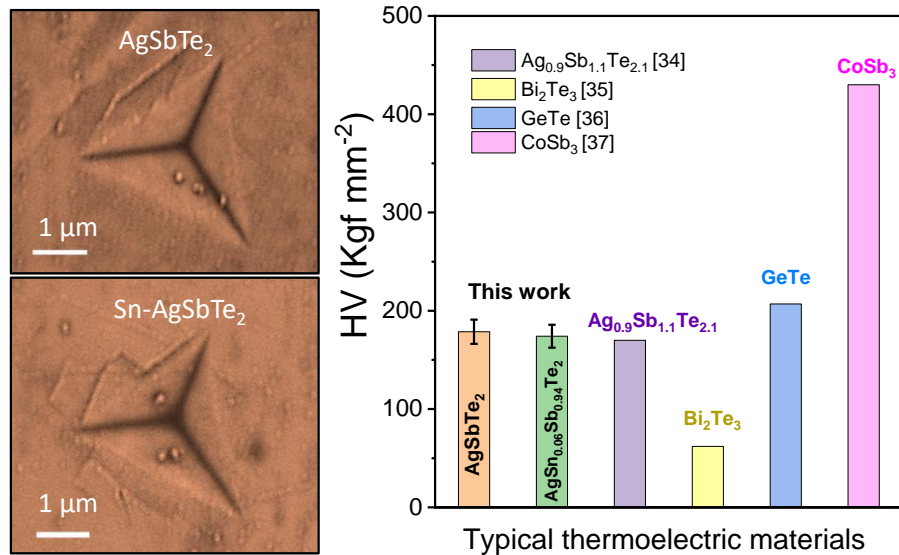
Supplementary Figure 17. **Mechanical Properties.** Comparisons on the Vickers hardness for $AgSbTe_2$ and $AgSb_{0.94}Sn_{0.06}Te_2$ with several typical TE materials. The Vickers hardness data are taken from references.[23-26]
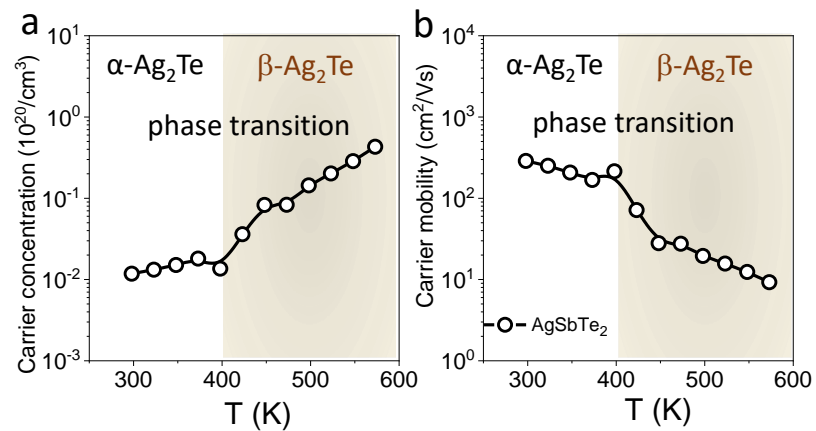
Supplementary Figure 18. **Carrier transport properties in pristine AgSbTe$_2$.** (a) Hall carrier concentration and (b) mobility of at temperatures 300-600 K in undoped AgSbTe$_2$.

Supplementary Table 1. Comparison of carrier density and mobility of $AgSbTe_2$ and $AgSb_{1-x}Sn_xTe_2$ samples at room temperature.

Sample	Charger carrier density (n_H, cm^{-3})	Charger carrier mobility (μ_H, cm^2/Vs)
$AgSbTe_2$	1.2×10^{18}	288.0
$AgSb_{0.97}Sn_{0.03}Te_2$	3.9×10^{19}	38.9
$AgSb_{0.94}Sn_{0.06}Te_2$	2.0×10^{19}	77.3
$AgSb_{0.9}Sn_{0.1}Te_2$	3.5×10^{19}	31.0

Supplementary Table 2. Density of $AgSbTe_2$ and $AgSb_{1-x}Sn_xTe_2$ samples

Sample	Density (g/cm3)	Relative density
$AgSbTe_2$	6.85	96.1 %
$AgSb_{0.97}Sn_{0.03}Te_2$	6.81	95.5 %
$AgSb_{0.94}Sn_{0.06}Te_2$	6.87	96.3 %
$AgSb_{0.9}Sn_{0.1}Te_2$	6.89	96.7 %

References

1   Zhang, K. *et al.* Dual Alloying Enables High Thermoelectric Performance in AgSbTe$_2$ by Manipulating Carrier Transport Behavior. *Adv. Funct. Mater.* 2400679 (2024).

2   Pan, Y. *et al.* Ultrahigh transverse thermoelectric power factor in flexible Weyl semimetal WTe$_2$. *Nat. Commun.* **13**, 3909 (2022).

3   Du, B., Li, H., Xu, J., Tang, X. & Uher, C. Enhanced figure-of-merit in Se-doped p-type AgSbTe$_2$ thermoelectric compound. *Chem. Mater.* **22**, 5521-5527 (2010).

4   Kim, S. I. *et al.* Dense dislocation arrays embedded in grain boundaries for high-performance bulk thermoelectrics. *Science* **348**, 109-114 (2015).

5   Zhou, C. *et al.* Polycrystalline SnSe with a thermoelectric figure of merit greater than the single crystal. *Nat. Mater.* **20**, 1378-1384 (2021).

6   Jiang, Y. *et al.* Evolution of defect structures leading to high ZT in GeTe-based thermoelectric materials. *Nat. Commun.* **13**, 6087 (2022).

7   Zong, P.-a. *et al.* Construction of a 3D-rGO network-wrapping architecture in a Yb$_y$Co$_4$Sb$_{12}$/rGO composite for enhancing the thermoelectric performance. *J. Mater. Chem.* **3**, 8643-8649 (2015).

8   Tan, G. *et al.* Non-equilibrium processing leads to record high thermoelectric figure of merit in PbTe-SrTe. *Nat. Commun.* **7**, 12167 (2016).

9   Hu, H. *et al.* Highly stabilized and efficient thermoelectric copper selenide. *Nat. Mater.* **23**, 527-534 (2024).

10 Roychowdhury, S. *et al.* Enhanced atomic ordering leads to high thermoelectric performance in AgSbTe$_2$. *Science* **371**, 722-727 (2021).

11 Ghosh, S. *et al.* High-entropy-driven half-Heusler alloys boost thermoelectric performance. *Joule* (2024).

12 Du, R. *et al.* Enhanced thermoelectric performance of Mg-doped AgSbTe$_2$ by inhibiting the formation of Ag$_2$Te. *ACS Appl. Mater. Interfaces.* **15**, 9508-9516 (2023).

13 Cao, J. *et al.* Non-equilibrium strategy for enhancing thermoelectric properties and improving stability of AgSbTe$_2$. *Nano Energy* **107**, 108118 (2023).

14 Lee, J. K. *et al.* Enhanced thermoelectric properties of AgSbTe$_2$ obtained by controlling heterophases with Ce doping. *Sci. Rep.* **7**, 4496 (2017).

15 Kim, J. H. *et al.* Enhancement of Phase Stability and Thermoelectric Performance of Meta-Stable AgSbTe2 by Thermal Cycling Process. *Adv. Funct. Mater.* 2404886 (2024).

16 Chen, B. C., Wang, K. K. & Wu, H. J. Cation Modulation in AgSbTe$_2$ Realizes Carrier Optimization, Defect Engineering, and a 7% Single-Leg Thermoelectric Efficiency. *Small*, 2401723 (2024).

17 Ganesan, P. *et al.* Carrier optimization and reduced thermal conductivity leading to enhanced thermoelectric performance in (Mg, S) co-doped AgSbTe$_2$. *Mater. Today Phys.* **42**, 101358 (2024).

18 Hong, M. *et al.* Achieving zT>2 in p-type AgSbTe$_{2-x}$Se$_x$ alloys via exploring the extra light valence band and introducing dense stacking faults. *Adv. Energy Mater.* **8**, 1702333 (2018).

19 Pathak, R. *et al.* Vacancy controlled nanoscale cation ordering leads to high thermoelectric performance. *Energy Environ. Sci.* **16**, 3110-3118 (2023).

20 Taneja, V. *et al.* High Thermoelectric Performance in Phonon-Glass Electron-Crystal Like AgSbTe$_2$. *Adv. Mater.* 2307058 (2024).

21 Bhui, A. *et al.* Hg Doping Induced Reduction in Structural Disorder Enhances the Thermoelectric Performance in AgSbTe2. *J. Am. Chem. Soc.* **145**, 25392-25400 (2023).

22 Zhang, Y. *et al.* Defect-engineering-stabilized AgSbTe$_2$ with high thermoelectric performance. *Adv. Mater.* **35**, 2208994 (2023).

23 Wu, Y. *et al.* High-performance and stable AgSbTe$_2$-based thermoelectric materials for near room temperature applications. *J Materiomics.* **8**, 1095-1103 (2022).

24 Perumal, S., Roychowdhury, S. & Biswas, K. Reduction of thermal conductivity through nanostructuring enhances the thermoelectric figure of merit in Ge$_{1-x}$Bi$_x$Te. *Inorg. Chem. Front.* **3**, 125-132 (2016).

25 Wang, D.-Z. *et al.* Simultaneously achieving high ZT and mechanical hardness in highly alloyed GeTe with symmetric nanodomains. *J. Chem. Eng.* **441**, 136131 (2022).

26 Dahal, T. *et al.* Thermoelectric and mechanical properties on misch metal filled p-type

skutterudites $Mm_{0.9}Fe_{4-x}Co_xSb_{12}$. *J. Appl. Phys.* **117** (2015).